Bilayer solid electrolyte enabling quasi-solid-state lithium-metal batteries

Fanglin Wu [a,b], Shan Fang [a,b], Matthias Kuenzel [a,b], Thomas Diemant [a,b], Jae-Kwang Kim [c,**], Dominic Bresser [a,b], Guk-Tae Kim [a,b,***], Stefano Passerini [a,b,*]

[a] Helmholtz Institute Ulm (HIU), Helmholtzstrasse 11, 89081, Ulm, Germany
[b] Karlsruhe Institute of Technology (KIT), P.O. Box 3640, 76021, Karlsruhe, Germany
[c] Department of Solar & Energy Engineering, Cheongju University, Cheongju, Chungbuk, 28503, Republic of Korea

GRAPHICAL ABSTRACT

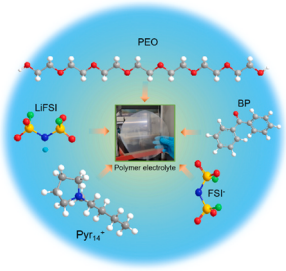

ARTICLE INFO

Keywords:
LAGP
Polymer
Solid electrolyte
Nickel-rich cathode
Lithium battery

ABSTRACT

NASICON-type electrolytes such as $Li_{1.5}Al_{0.5}Ge_{1.5}(PO_4)_3$ (LAGP) potentially enable high safety and high energy for solid-state batteries. However, the poor interfacial stability with lithium metal remains a main issue. To overcome this challenge, we proposed a bilayer solid electrolyte architecture implementing a novel ultrathin solid polymer electrolyte (SPE) film in combination with LAGP to improve the interface with lithium metal. The SPE film is composed of a bis(fluorosulfonyl)imide-based ionic liquid and polyethylene oxide, which shows a remarkable ionic conductivity of 1.25×10^{-3} S cm^{-1} at room temperature. The application of this thin interlayer leads to an outstanding interface stability, allowing >2000 h of continuous Li stripping/plating in symmetric Li|SPE/LAGP/SPE|Li cells without any increase in polarization or indication of a short circuit. As a result, this approach enables Li|SPE/LAGP|NCM811 cells with a discharge capacity of ~200 mAh g^{-1} at 0.1C and stable cycling for >400 cycles at 0.2C with a capacity retention of 83%. Additionally, the cell shows an extremely high average Coulombic efficiency of 99.96% demonstrating that the approach enables to achieve high-energy and long-term stable solid-state lithium-metal batteries.

* Corresponding author. Helmholtz Institute Ulm (HIU), Helmholtzstrasse 11, 89081, Ulm, Germany.
** Corresponding author.
*** Corresponding author. Helmholtz Institute Ulm (HIU), Helmholtzstrasse 11, 89081, Ulm, Germany.
E-mail addresses: jaekwang@cju.ac.kr (J.-K. Kim), guk-tae.kim@kit.edu (G.-T. Kim), stefano.passerini@kit.edu (S. Passerini).

1. Introduction

Since a few years, lithium-metal batteries (LMBs) have regained attention in academia and industry as they promise superior energy density due to the high specific capacity and low electrochemical potential of lithium metal [1–3]. Nevertheless, the severe safety concerns associated to dendritic lithium growth and the rather low Coulombic efficiency in conventional liquid electrolytes hinder the practical implementation of LMBs [4,5]. One approach to overcome these challenges is the replacement of the (frequently flammable) liquid electrolyte by an intrinsically safer alternative such as solid inorganic electrolytes. Among these, NASICON-type lithium metal phosphates like $Li_{1.5}Al_{0.5}Ge_{1.5}(PO_4)_3$ (LAGP) [6–8] or $Li_{1.3}Al_{0.3}Ti_{1.7}(PO_4)_3$ (LATP) [9] have received great attention for their good ionic conductivity (~10^{-4} S cm^{-1}) and wide electrochemical stability window (up to 6 V) [10]. Furthermore, LAGP is very stable against moisture and oxygen [11], which is a great advantage for both electrolyte processing and battery cell assembly. However, it suffers a rather poor stability against lithium metal owing to the reduction of Ge^{4+}, thus, forming a mixed ion and electron conducting interphase [12,13]. Besides, the reduction of Ge^{4+} severely affects the mechanical integrity of the solid electrolyte (SE), finally causing its pulverization and failure of the cell [13,14].

Recently, a few studies have attempted to address this issue. For instance, Zhou et al. [15] sputtered a thin film of amorphous germanium (~60 nm) onto the LAGP surface and demonstrated that this metallic germanium film suppresses the reduction of Ge^{4+} inside the LAGP, while simultaneously forming an intimate lithium conducting layer between the SE and the lithium metal. Similarly, Sun et al. [16] deposited a thin Al_2O_3 layer onto LATP, which led to an improved cycling stability for 600 h owing to the low interfacial impedance, the suppressed Ti^{4+} reduction, and the formation of a lithium conducting Li–Al–O layer at the Li|LATP interface. Following these attempts, Li et al. [10] adopted an *in situ* solidification method to form an ion conducting, but electronically insulating interlayer with $Li_{6.4}La_3Zr_2Al_{0.24}O_{12}$ nanowires to avoid the side reactions between LAGP and lithium metal. Additionally, the three dimensional (3D) ion conduction within this interphase supported a homogenous lithium deposition.

Another approach that has been reported recently relies on the use of ion conducting polymer interlayers to protect the SE against the lithium metal. Li and co-workers [17], for instance, designed a 100 µm thick gel-polymer electrolyte to stabilize the Li|LAGP interface and achieved a good cycling stability of Li//$LiFePO_4$ cells for 300 cycles at room temperature. In a later study, Xu et al. [18] designed a tri-layer SE structure that consisted of a relatively thicker, porous LAGP layer to host the $LiNi_{0.8}Co_{0.1}Mn_{0.1}O_2$ (NCM811) active material, a thin and dense LAGP layer as Li^+ conducting electrolyte, and a layer of polyethylene glycol bis (amine)-triglycidyl isocyanurate. The combination with a lithium-metal negative electrode allowed for a high areal capacity of 2 mAh cm^{-2} at 0.1C and a capacity retention of 70% after 50 cycles. Nonetheless, long term performance is still not achieved calling for the further improvement of the interphase between LAGP and lithium metal. Herein, we propose a new design employing a very thin (≤20 µm) solid polymer-based electrolyte layer with high ionic conductivity using polyethylene oxide (PEO) that was crosslinked with benzophenone (BP) as photo-initiator and comprised a bis(fluorosulfonyl)imide (FSI)-based ionic liquid (IL) to support the charge transfer and optimize the electro-/chemical properties. A scheme of the polymer electrolyte fabrication is depicted in Fig. 1a. In general, solid polymer electrolytes typically feature ionic conductivities below 10^{-4} S cm^{-1} [14], this newly designed SPE, however, displays a much superior ionic conductivity of up to 1.25×10^{-3} S cm^{-1}, which is at least the highest ionic conductivity reported for PEO-based solid polymer electrolytes, if not even the highest among all solid polymer electrolytes, to the best of our knowledge [19–23]. The charge transfer as well as the interfacial contact and stability at both electrode|electrolyte interfaces is further enhanced by adding one drop (≤5 µL) of non-flammable $0.8Pyr_{14}FSI$-0.2LiTFSI on the two electrodes, respectively, following a previous approach [24]. The eventual Li|SPE/LAGP|NCM811 full-cell setup is compared with the conventional Li|LAGP|NCM811 setup in Fig. 1b and c. It is found that this advanced cell design suppresses the Ge^{4+} reduction and dendrite formation owing to the stabilized solid electrolyte interphase (SEI) formed between the 2D bilayer electrolyte and the lithium-metal anode, resulting in a substantially decreased interfacial impedance. These advantageous properties finally yield an unprecedented cycling stability and outstanding Coulombic efficiency of these high-energy quasi-solid-state Li-metal cells.

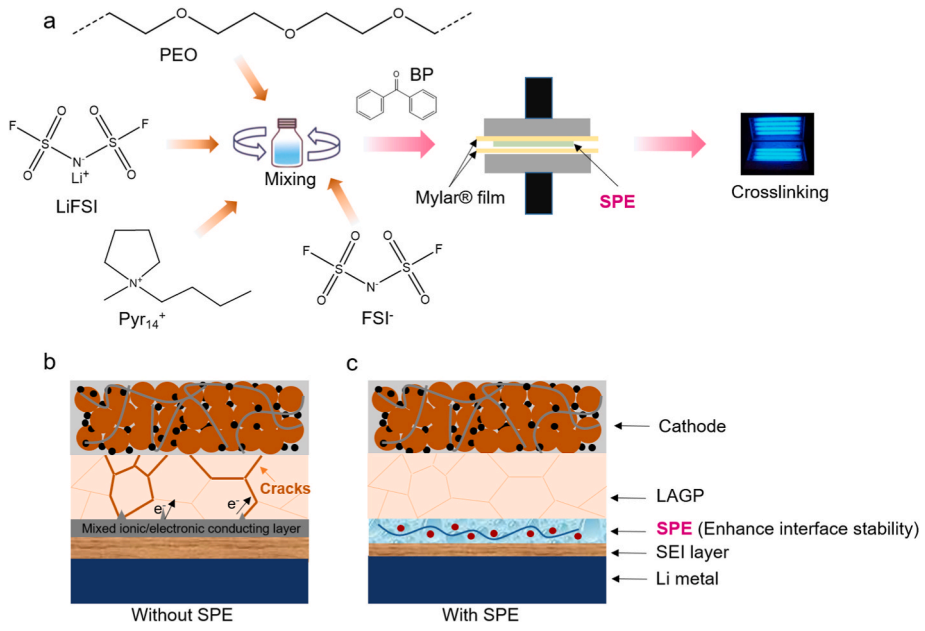

Fig. 1. Preparation of the SPE interlayer for quasi-solid-state batteries. (a) Process to prepare a thin ionic liquid containing solid polymer electrolyte. (b,c) Schematic illustration of Li|LAGP|NCM811 (quasi-)solid-state batteries (b) without and (c) with the SPE interlayer.

2. Results and discussion

$Li_{1.5}Al_{0.5}Ge_{1.5}(PO_4)_3$ (LAGP) was synthesized *via* a solid state reaction as described in the Experimental section. The resulting powder reveals primary particles (mostly less than 1 μm) of irregular polyhedral morphology agglomerated into micrometer-sized secondary particles (**Fig. S1**). X-ray diffraction (XRD) confirms that the obtained material has the designated NASICON-type $Li_{1.5}Al_{0.5}Ge_{1.5}(PO_4)_3$ phase with some minor contribution from an $AlPO_4$ phase (PDF card #00-011-0500, Fig. 2a). In a next step, the pellets were sintered at different temperatures in the range from 850 °C to 1000 °C to identify a suitable compromise between the various temperature-affected properties such as grain size, porosity, and density in order to maximize the overall ionic conductivity. Photographs of the sintered pellets are displayed in Fig. S2a and the plots of the electrochemical impedance spectroscopy (EIS) data are presented in Fig. S2b and summarized in Table S1. The pellets sintered at 900 °C showed the lowest bulk impedance of 329.2 Ω and, thus, the highest ionic conductivity of 3.25×10^{-4} S cm^{-1} (see also Fig. 2b). Accordingly, this sintering temperature was chosen for all further experiments. A scanning electron microscopy (SEM) image of the resulting pellet is presented in Fig. 2c, revealing densely agglomerated primary particles, which likely contributes to the rather high ionic conductivity. This is confirmed by the cross-sectional SEM analysis (**Figs. S3a and b**), which also shows that the thickness of the sintered pellets is about 600 μm under the given conditions. In fact, especially after polishing the cross-section with the focused ion beam (Fig. S3c), it becomes apparent that the porosity in such pellets is very minor and limited to a few well separated pores, while the contact between the agglomerated primary particles is very intimate. Moreover, the SEM and energy dispersive X-ray spectroscopy (EDX) investigation of the polished cross-section (Figs. S3c and d) reveals some darker grains that turn out to be aluminium-rich and essentially free of germanium, indicating that these grains correspond to the $AlPO_4$ phase detected *via* XRD (Fig. 2a), which was thought to act as space charge mediator to improve the solid eletrolyte's conductivity [25–28].

To avoid the direct contact between the LAGP pellet and lithium metal and to enhance the interfacial contact, a thin polymer-based electrolyte was used (see Fig. S4a) showing excellent flexibility (Figs. S4b–d) and excellent ionic conductivity of 1.25×10^{-3} S cm^{-1} at room temperature, i.e., a bulk resistance of only 1.59 Ω (see Fig. 2d). At 40 and 80 °C the ionic conductivity further increases to ~2×10^{-3} S cm^{-1} and ~5×10^{-3} S cm^{-1}, respectively (Fig. 2e), i.e., values that are comparable to most electrolytes based on ionic liquids only [29]. Such a high conductivity is assigned to the incorporation of the FSI anion instead of the commonly used bis(trifluoromethanesulfonyl)imide (TFSI) [22]. In a next step, we calculated the (apparent) activation energy for the SPE and LAGP using, respectively, the Vogel–Fulcher–Tammann (VFT) equation or the Arrhenius equation [30], yielding values of 0.09 eV (Fig. 2e) and 0.36 eV (Fig. S5a), respectively, i.e., a lower value for the SPE. Nonetheless, the overall charge transport in solid-state batteries is largely determined by the charge transfer across the different interfaces [31] – especially in such bilayer systems with two different ion-conducting phases in series. To probe the interfacial resistance between the SPE and the LAGP phase, we assembled Cu/Pt|LAGP|Pt/Cu and Cu/Pt|LAGP/SPE|Cu cells, subjected both to EIS, and compared the resulting Nyquist plots in **Fig. S5b**. The overall resistance is very similar, suggesting for the negligible impact of the additional SPE layer, resulting from its rather low ionic resistance.

Finally, we also evaluated the thermal stability by thermogravimetric analysis (TGA) to get a first hint regarding the intrinsic safety of such bilayer quasi-solid-state electrolyte system, the results are presented in Fig. 2f. Neat LAGP does not show any significant mass loss up to 600 °C, while neat SPE is stable up to 215 °C, which is by far superior to conventional liquid organic electrolytes [32]. Furthermore, the SPE-coated LAGP still maintains its good thermal stability (see Fig. S6).

To confirm the performance of the bilayer SPE/LAGP electrolyte, a series of lithium stripping/plating experiments were performed using different cell configurations, as summarized in Fig. 3. The Li|LAGP|Li

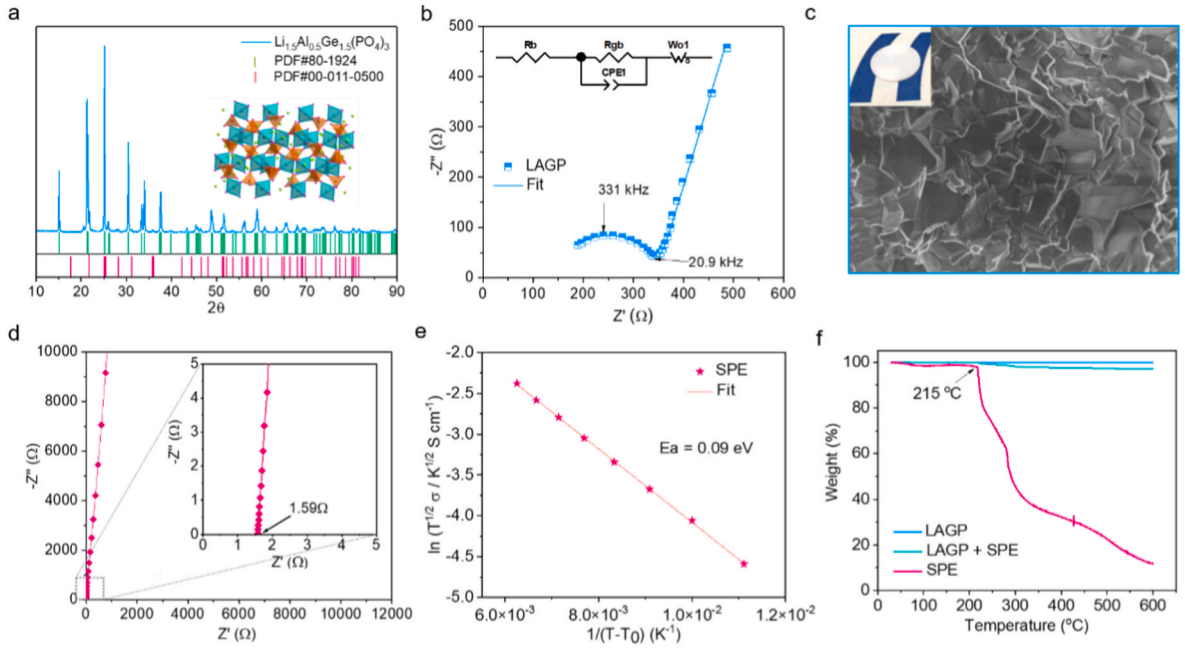

Fig. 2. Characterization of the LAGP and the polymer-based electrolyte. (a) XRD pattern of the LAGP powder, including the PDF references for $LiGe_2(PO_4)_3$ (PDF card #80–1924, in light green) and $AlPO_4$ (PDF card #00-011-0500, in red) for comparison. (b) EIS-derived Nyquist plot obtained for the symmetric Cu/Pt|LAGP|Pt/Cu cell at room temperature and the corresponding fit; the utilized equivalent circuit is provided as inset. (c) SEM micrograph of the LAGP pellet; the inset shows a photograph of the LAGP pellet sintered at 900 °C. (d) EIS-derived Nyquist plot of the symmetric Cu|SPE|Cu cell at room temperature; a magnification of the high frequency range is provided as inset. (e) Plot of the ionic conductivity as a function of temperature and the corresponding fit using the VFT equation to yield the (apparent) activation energy of SPE. (f) TGA of LAGP, SPE, and the bilayer solid electrolyte. (For interpretation of the references to color in this figure legend, the reader is referred to the Web version of this article.)

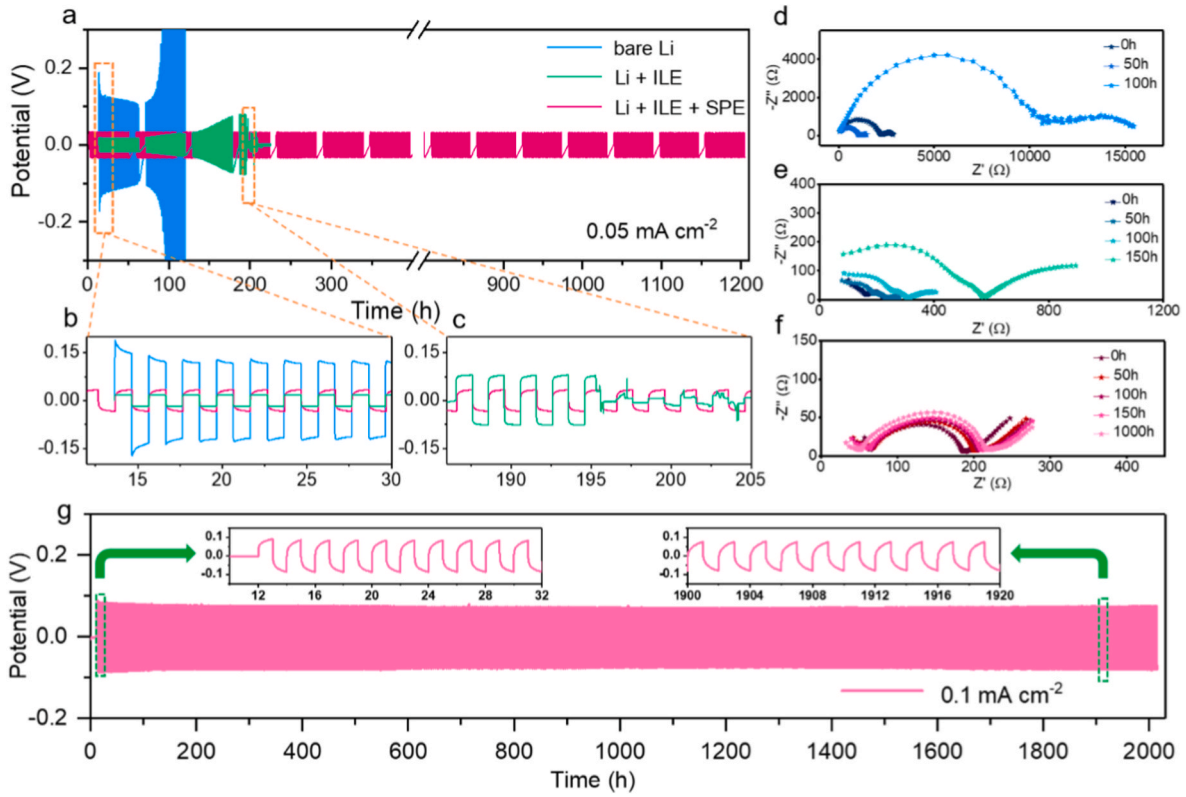

Fig. 3. Impact of the ILE and SPE on the lithium stripping/plating behavior of LAGP-based solid-state batteries. (a) Long-term galvanostatic stripping/plating experiment for Li|LAGP|Li (in light blue), Li|ILE/LAGP/ILE|Li (in light green), and Li|ILE/SPE/LAGP/SPE/ILE|Li (in red) cells with a constant current density of 0.05 mA cm^{-2} (with each stripping and plating step lasting for 2 h and an OCV step after each 12 h). (b,c) Magnification of the corresponding voltage profiles as indicated in (a). (d–f) Evolution of the EIS-derived Nyquist plots upon continuous stripping and plating for (d) the Li|LAGP|Li cells, (e) the Li|ILE/LAGP/ILE|Li cells, and (f) the Li|ILE/SPE/LAGP/SPE/ILE|Li cells. (g) Ultra-long-term galvanostatic stripping/plating experiment for Li|ILE/SPE/LAGP/SPE/ILE|Li cells with a constant current density of 0.1 mA cm^{-2}. (For interpretation of the references to color in this figure legend, the reader is referred to the Web version of this article.)

cells present a relatively high overpotential, reaching initially almost 0.2 V at an applied current density of 0.05 mA cm^{-2} (Fig. 3a and b), due to the poor solid-solid interface contact. Upon cycling, the overpotential drops steadily to stabilize at around 0.1 V resulting from the increasing contact area between LAGP and Li. Finally, a significant increase is observed after about 80 h (Fig. 3a). The same phenomenon was already reported before [15] and is presumably related to the reduction of LAGP in contact with the lithium metal, leading to fast Li|LAGP|Li cell failure. Differently, the Li|ILE/LAGP/ILE|Li cells, which electrodes were wet with a drop of an ionic liquid-based electrolyte (ILE, 0.8PYR_{14}FSI-0.2-LiTFSI), show a much lower overpotential (<0.02 V) along the continuous stripping and plating (Fig. 3a and b). However, a gradual increase is visible after about 150 h, suggesting an increase of the impedance at the interface between lithium metal and LAGP in these Li|ILE/LAGP/ILE|Li cells (Fig. 3a). After about 195 h the overpotential drops to 0 V (Fig. 3c), which is assigned to the formation of lithium dendrites along microcracks in the LAGP pellets short-circuiting the cell. Apparently, the addition of ILE is not sufficient to suppress the dendritic growth of Li and the side reaction at the Li|LAGP interface, which is in line with previous findings [24,33]. In contrast, the ultra-thin SPE protection layer allows for a dramatically improved long-term cycling stability of Li|ILE/SPE/LAGP/SPE/ILE|Li cells (Fig. 3a–c) without any visible change of the overpotential (about 0.03 V) even after 1000 h of lithium stripping and plating. This demonstrates that a highly stable interphase is formed between Li and the SPE-protected LAGP. To further evaluate the impact of ILE and SPE on the interfacial stability, EIS was performed on the different cells to follow the evolution of the impedance upon stripping and plating at 0.05 mA cm^{-2} (Fig. 3d–f). For the Li|LAGP|Li cells, the initial impedance of 2186 Ω decreases to 1077 Ω after 50 h and then jumps to 10,908 Ω after 100 h (Fig. 3d). In contrast, the initial overall resistance is significantly reduced to only 153 Ω in the presence of ILE, but continuously increases upon stripping and plating (**Fig. 3e**). The Li|ILE/SPE/LAGP/SPE/ILE|Li cell shows only a slightly higher initial impedance (189 Ω, Fig. 3f), indicating that the SPE has only a minor impact on the cell impedance. Even more important, the impedance remains very stable showing no significant increase upon 1000 h of stripping and plating. This excellent interfacial stability is further highlighted by the stripping/plating test at higher current (0.1 mA cm^{-2}). Once more, no appreciable increase in overpotential is observed – even after more than 2000 h (Fig. 3g). The magnification of the voltage profiles at the beginning and towards the end of the experiment (provided as insets) further supports this excellent interfacial stability, as the overpotential remains extremely stable and below 0.1 V throughout the whole experiment. The interfacial stability of Li|ILE/SPE/LAGP/SPE/ILE|Li cells was also examined at different current densities increasing from 0.05 mA cm^{-2} to 0.3 mA cm^{-2}. As expected, the overpotential grew significantly with every current increase (Fig. S7) and, at the highest current levels, the cell potential overshoots before gradually stabilize within a few cycles. However, no cell failure was observed, proving that the SPE interlayer plays a key role in protecting LAGP against lithium metal and that it effectively suppresses the formation of lithium dendrites.

The excellent performance of Li|ILE/SPE/LAGP/SPE/ILE|Li cells lays the foundation for the realization of LAGP-based, quasi-solid-state lithium-metal batteries employing state-of-the-art high-energy, nickel-rich layered oxide cathode materials such as $LiNi_{0.8}Co_{0.1}Mn_{0.1}O_2$ (NCM811). To ensure a good ionic contact also between the LAGP and the NCM811-based cathodes, one drop of the tailored ILE (i.e., 0.8PYR_{14}FSI-0.2LiTFSI) was added onto the surface of the positive electrode. In fact, we have shown in previous studies that this dual-ion

ILE provides a wide electrochemical stability window and forms a beneficial cathode|electrolyte interphase layer for high-voltage lithium-rich cathodes [34] and nickel-rich cathodes [35]. The electrochemical performance of the resulting Li|ILE/SPE/LAGP/ILE|NCM811 cells is compared in Fig. 4 with that of Li|ILE/LAGP/ILE|NCM811 cells, i.e., with and without the SPE interlayer. The cells were galvanostatically charged and discharged at a rate of 0.1C for the initial two cycles and subsequently cycled at 0.2C. The comparison of the first cycle voltage profiles is displayed in Fig. S8. The charge profiles essentially coincide for the two different cell setups, apart from a slightly lower specific capacity of the SPE-comprising cell (217 mAh g ^{1} vs. 220 mAh g ^{1}). The capacity difference increases slightly at the end of the first discharge (199 mAh g ^{1} vs. 204 mAh g ^{1}) and is also reflected in the first cycle Coulombic efficiency (CE), which is slightly lower for the SPE-containing cell (88.6% vs. 92.7%). A possible explanation for this capacity loss and lower CE might be some contribution to the SEI layer formation on the SPE layer during the initial charge process, which will be further discussed later (see X-ray photoelectron spectroscopy (XPS) analysis). Upon the subsequent constant current cycling at 0.2C, however, the SPE-protected cell shows a dramatically enhanced cycling stability without any performance decay and the CE remains very close to 100% throughout the cycling test (Fig. 4a). In contrast, the cell without the SPE interlayer shows a relatively stable capacity only for about 10 cycles, before the capacity drops rapidly, furthermore, a decreased and fluctuating CE is noticed. This is associated to the spontaneous reduction reaction occurring at the LAGP and Li metal interface and forming a mixed ionic/electronic conducting interphase layer (black color), but also leading to the mechanical degradation of LAGP, finally resulting in the pulverization of the pellet (see the optical images in Fig. S9). In contrast, the bilayer SPE/SE electrolyte appears to be intact, proving the ability of SPE to prevent the destructive reaction between LAGP and Li as well as lithium dendrites growth [13]. The comparison of the performance herein achieved with that of state-of-art (quasi)solid--state lithium metal batteries (Fig. 4e) demonstrates the neat advantage of the SPE/SE electrolyte, especially when high-voltage layered cathodes are concerned.

The rate capability of the quasi-solid-state Li|ILE/SPE/LAGP/ILE|NCM811 cells was probed at different C rates ranging from 0.1C to 1C (Fig. 4b). The results show that even at a rather high current density of 100 mA g ^{1} a specific capacity of 153 mAh g ^{1} was maintained. After

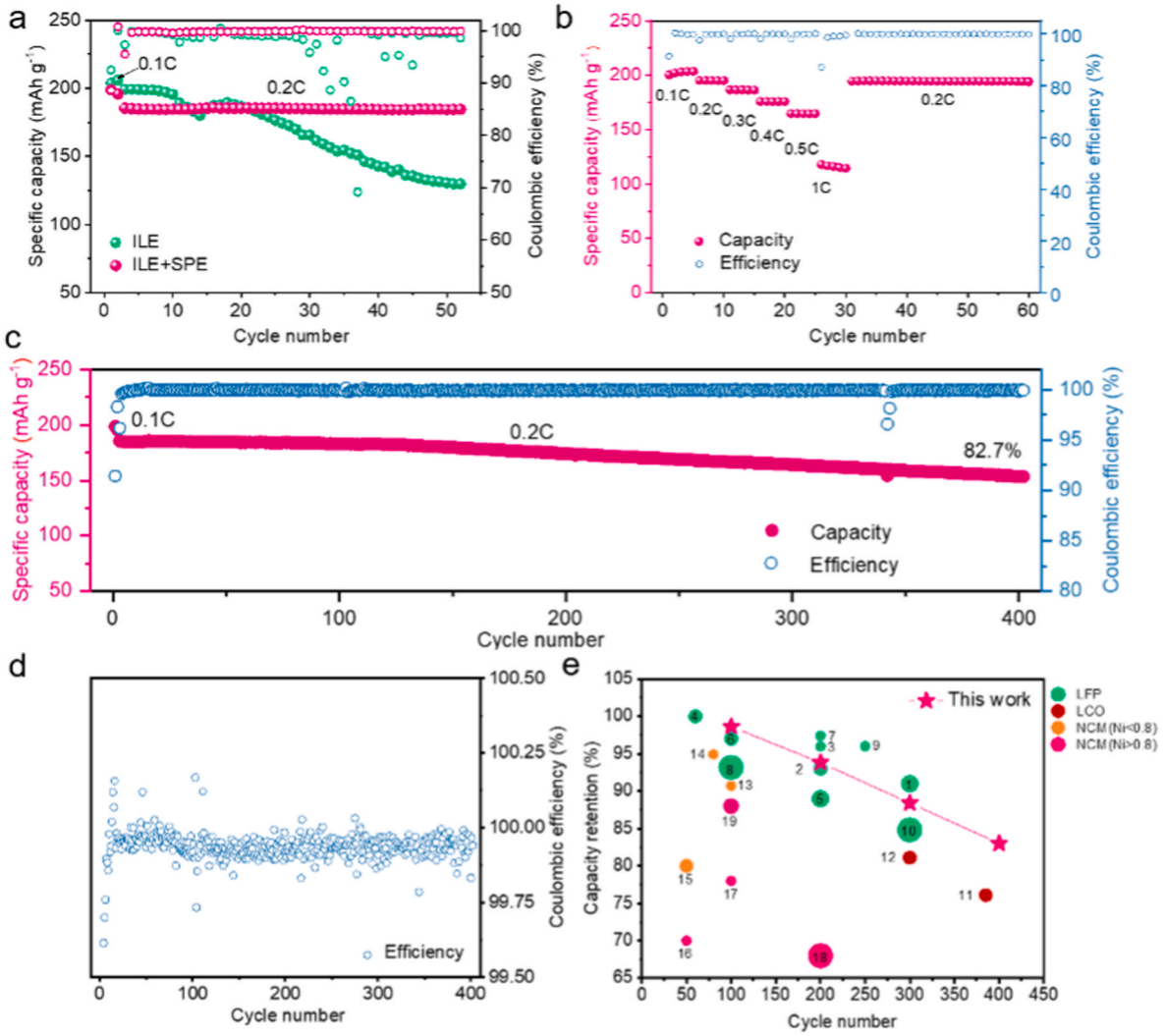

Fig. 4. Electrochemical performance of quasi-solid-state Li||NCM811 cells. (a) Comparison of the constant current cycling stability of LAGP-based Li||NCM811 cells with (red) and without (green) the SPE interlayer on the LAGP at 0.2C. All cells were subjected to two formation cycles at 0.1C. (b) Rate capability and (c) long-term constant current (0.2C) cycling of the Li|SPE/LAGP|NCM811 cells. (d) Magnification of the CE values corresponding to experiment presented in (c). (e) Cycling stability (capacity retention vs number of cycles) of (quasi)solid-state Li-metal cells based on oxide-type SE or SPE. Further details are reported in Table S2 [10,17, 36–48]. Finally, the size of the markers is proportional to the current rate used for the tests. All electrochemical tests were conducted at 40 °C. (For interpretation of the references to color in this figure legend, the reader is referred to the Web version of this article.)

the rate test, the initial specific capacity at 0.2C rate was recovered (190 mAh g ^{1} at 0.2C) associated with excellent cycling stability. The C-rate performance tests of Li|*ILE/LAGP/ILE*|NCM811 cells, i.e., without the SPE interlayer protection, showed similar performance especially at high current density (Fig. S10), suggesting that the SPE interlayer is not the barrier for fast charge. Further, the SPE-free cell shows obvious capacity fading and fluctuating Coulombic efficiency confirming the importance of SPE interlayer to the stability of cells. These findings corroborate the effectiveness of the thin SPE layer in protecting LAGP. Eventually, long-term cycling was carried out at 0.2C, as presented in Fig. 4c. A remarkable cycling stability was achieved with a capacity retention of 82.7% after 400 cycles. Even more remarkable, the cells display an exceptionally high CE that averages to about 99.96% (Fig. 4d). To evaluate the environmental suitability of SPE-protected cells within an extended temperature range, Li-metal full cells were also tested at lower (30 °C, Fig. S11) and higher (60 °C, Fig. S12) temperatures. At 30 °C, the cell delivered a specific capacity of 180 mAh g ^{1} at 0.1C and showed high cycling stability for about 200 cycles. More interestingly, a remarkable performance is also observed at 60 °C, e.g., a specific capacity of 175 mAh g ^{1} could be noted even at the relatively high current rate of 200 mA g ^{1} (1C) together with an outstanding stability with a capacity retention of 96.3% over 200 cycles. Furthermore, a preliminary measurement was also conducted to evaluate the practical relevance of this quasi-solid state lithium metal batteries, a high areal capacity (>2 mAh cm ^{2}) was achieved using high loading NCM811 electrode (~12 mg cm ^{2}), as shown in Fig. S13. These results demonstrate that the quasi-solid state lithium metal cell features superior high-temperature resistance. Safety is also an indispensable factor in evaluating the properties of solid-state lithium metal batteries. As a rough test, the pouch cell lighting a LED bulb at room temperature (Fig. S14) did not show any notable failure under the harsh condition of bending or cutting. Finally, no ignition was observed even when the cell was exposed to fire, which proves the outstanding non-flammability of this quasi-solid state lithium metal system.

To determine the effect of SPE on the electrodes, Li//NCM811 cells were disassembled after 50 cycles and the morphology of the Li-metal and NCM811 electrodes was investigated by post mortem SEM analysis, as shown in Fig. 5. The Li-metal surface without SPE protection presents a rugged morphology (Fig. 5a). A closer look (Fig. 5b) shows that small areas of unreacted Li-metal persist, however, most of the surface is covered by the side reaction products of the severe reaction with LAGP. The image taken at the edge of the Li metal electrode show the difference between the pristine metal and that reacted with LAGP (Fig. S15). In contrast, the Li-metal with SPE protection exhibits a highly dense and smooth surface, which clearly demonstrates the outstanding protective function of SPE interlayer as well as a robust SEI layer formation (Fig. 5 e-f). Regarding the NCM811 electrodes, the presence of the SPE interlayer does not induce large differences. Nonetheless, the magnified SEM images reveal some changes occurring on the particle surface of the electrode without the SPE interlayer (Fig. 5d); the surface was obviously covered by a thick amorphous layer (e.g., the part in Fig. 5d marked with green circle), probably due to the deposition of decomposition products between the cathode and electrolyte, which aggravated the cathode electrolyte interphase layer formed at higher interface resistance. Furthermore, a large crack is presented clearly in the particle (green rectangle). In contrast, the sample with SPE protection shows a clean surface and intact morphology (Fig. 5g and h), these differences are most likely due to inhomogeneous current distribution due to the non-homogeneous lithium plating and stripping at the negative electrode.

Having proven the advantageous effect of the SPE layer, the focus shifted on the understanding of such a beneficial impact, further investigating the interaction of the SPE layer with the lithium metal and the LAGP. For this purpose, the surface of the lithium electrode and the LAGP pellet as well as the SPE layer itself were investigated by *ex situ* XPS. Fig. 6 shows selected detail spectra regarding the SEI composition

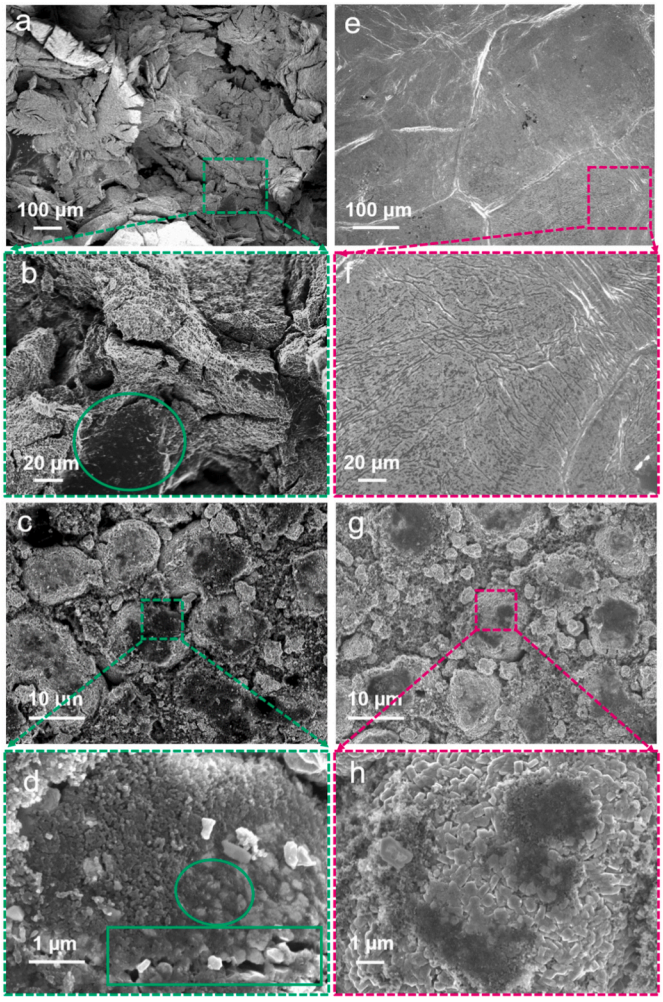

Fig. 5. SEM micrographs of Li-metal (a,b,e,f) and NCM811 (c,d,g,h) electrodes after 50 cycles at 0.2C and 40 °C. (a–d) without SPE interlayer protection (i.e., Li|ILE/LAGP/ILE|NCM811), (e–h) with SPE interlayer protection (i.e., Li|ILE/SPE/LAGP/ILE|NCM811).

(F1s, N1s, and S2p) on the lithium electrodes recovered from symmetric cells (with and without SPE) after prolonged stripping/plating for 1000 h at 0.05 mA cm ^{2}. It should be noted that the SPE-comprising sample was measured again after removing the top layer material by Ar^{+} sputtering to gain more information about the composition in deeper layers. Starting with the spectra in the F1s range, three peaks at 688.8, 687.2 and 685.0 eV were detected, which belong to TFSI and FSI groups from the ILE and SPE, and to LiF, respectively. While the intensity of the first two signals (TFSI and FSI) is rather similar for both electrodes (without and with SPE), the LiF peak intensity differs substantially, being much stronger in the SPE-free electrode. Since LiF derives from the decomposition of the electrolyte in contact with lithium metal [49], the stronger peak indicates a higher amount of decomposition products on the lithium metal surface in the absence of SPE, i.e., a thicker SEI layer. In direct comparison, the LiF peak on the surface of the SPE-protected electrode is less intense, becoming more pronounced only after sputtering, i.e., in greater depths or closer to the Li-metal surface. This suggests that the SPE interlayer is beneficial to hinder an excessive growth of the SEI layer by suppressing the decomposition reaction of the electrolyte with the lithium metal. In the N1s region, besides the peaks from ILE and SPE, a strong peak corresponding to Li_3N is observed for the sample without SPE, which is characteristic for the decomposition of the ILE in contact with lithium metal [50]. As a matter of fact, there is no such Li_3N species observed in the outer SEI layer for the SPE-protected

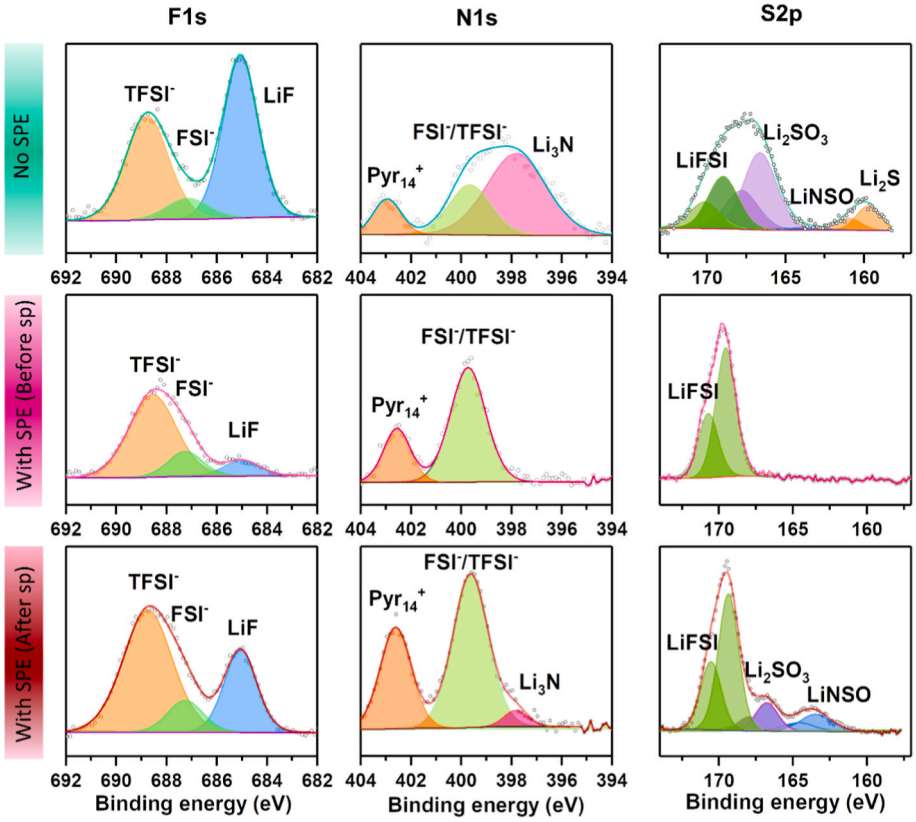

Fig. 6. Characterization of the SEI on the lithium electrode surface after cycling via ex situ XPS. The spectra were recorded after continuous stripping/plating for 1000 h (0.05 mA cm^{-2}; each stripping and plating step lasted for 2 h) in symmetric Li|ILE/LAGP/ILE|Li (top) and Li|ILE/SPE/LAGP/SPE/ILE|Li (middle and bottom) cells. In the latter case, the SPE interlayer was removed and the measurements were performed before (middle) and after sputtering (bottom).

electrode. Only a minor Li_3N contribution is detected in the inner SEI layer after sputtering. The same behavior is observed in the S2p region, where a series of sulfite and sulfide products is found on the unprotected lithium electrode, while only minor amounts of such species are found in the deeper SEI layer of the SPE-protected Li electrode. In general, such inorganic components (e.g., Li_3N and sulfite) are beneficial to build a robust SEI layer. However, in the present case, it appears to be not enough to suppress the reduction of LAGP by lithium metal, meanwhile the continuous ILE decomposition as well as the formation of mixed ionic/electronic conducting interphase layer leads to increasing cell impedance (see also Fig. 3e).

The surface of LAGP and SPE were also investigated by XPS (see Fig. S16 and Fig. S17, respectively). Summarizing the findings for the components of the cell employing the SPE-interlayer, it can be concluded that in the surface of all materials (Li metal, SPE, LAGP) the S2p spectra are dominated by the FSI peak, while sulfite species occur only in the inner surface layer (i.e., after sputtering), which means that these species are only generated at the early stage of cycling. This, in turn, means that ILE only decomposes initially, forming some sulfite species, LiF, and others, stabilizing the interface with the LAGP and lithium metal, and suppressing the formation of lithium dendrites. Afterwards, there are no further decomposition products deposited on the surface of LAGP, SPE, and Li metal, indicating that the formed interphases are stable. Additionally, no germanium reduction products were detected on the LAGP surface (Fig. S18), demonstrating the effective protection of the SPE interlayer between LAGP and Li metal. In the case of the SPE-free cell, however, strong peaks of decomposition products are detected in the spectra of the lithium metal surface, which are not observed on the LAGP surface (Fig. S16). Only LiF is found, but in a clearly lower amount than in the case of the LAGP from the SPE-coated cell, indicating that the decomposition products do not protect the LAGP effectively, but they just accumulate on the Li metal surface to form a thick and unstable SEI layer.

3. Conclusion

In this work, a novel, quasi-solid-state electrolyte is reported which enables the long-term cycling of Li metal batteries. The electrolyte makes use of the NASICON-type LAGP, which is protected against the lithium metal anode by a thin layer of polymer electrolyte. Such a bilayer electrolyte ensures an outstanding cycling stability and excellently stable interfacial impedance. These remarkable features are attributed to the high R.T. ionic conductivity of 1.25×10^{-3} S cm^{-1} as well as excellent flexibility and mechanical strength of the SPE interlayer. In details, the interlayer helps to overcome the poor interfacial contact between SE and Li metal owing to its high flexibility, dramatically reducing the interfacial resistance. Despite being only few micrometres thick, the SPE interlayer effectively acts as a physical barrier to avoid any direct electronic contact between LAGP and lithium metal, i.e., preventing the reduction of Ge^{4+} and supressing the growth of lithium dendrites. This latter phenomenon is regarded as the main reason for the interfacial instability of NASICON-type SEs in lithium-metal batteries. Accordingly, the thin polymer electrolyte interlayer with high ionic conductivity provides a promising route to relieve the interfacial instability of LAGP in contact with lithium metal and allows for the realization of high-energy quasi-solid-state lithium-metal battery cells with long cycle life. We may anticipate that this approach can be extended also to other inorganic SEs suffering of interface issues – with both the positive and/or the negative electrode – and, thus, provide a promising, cost-efficient, and easily implementable strategy towards intrinsically safer high-energy lithium-metal batteries.

4. Experimental part

Preparation of the LAGP pellets: $Li_{1.5}Al_{0.5}Ge_{1.5}(PO_4)_3$ (LAGP) was synthesized *via* a simple solid state reaction. Stoichiometric amounts of Li_2CO_3 (≥99.0%, EMSURE® ACS, 10% excess), $Al(NO_3)_3{\cdot}9H_2O$ (99+%, ACROS ORGANICS), GeO_2 (99.998%, Aldrich), and $(NH_4)H_2PO_4$ (≥99.0%, EMSURE® ACS) were mixed in ethanol and ball-milled in ZrO_2 jars for 2 h at 720 rpm. Subsequently, the solvent was removed using a rotary evaporator and the remaining powder was dried in an oven at 80 °C overnight. The powder was pretreated at 400 °C for 5 h (heating ramp: 5 °C min^{-1}), collected and ground, and eventually calcined at 800 °C for 8 h (heating ramp: 5 °C min^{-1}). The calcined powder was ball-milled again at 1400 rpm for 2 h to obtain the final product. For the preparation of pellets, the powder was filled into a 15 mm die and pressed at 3 t cm^{-2}. The resulting pellet was pretreated at 400 °C for 2 h (heating ramp: 3 °C min^{-1}) and finally sintered at 900 °C for 8 h (heating ramp: 5 °C min^{-1}). The sintered pellets were polished to a thickness of around 0.6 mm and ultrasonically cleaned before drying the once more at 100 °C for 12 h.

Preparation of the polymer electrolyte comprising the ionic liquid: The ionic liquid-containing polymer electrolyte was prepared *via* a solvent-free method. Polyethylene oxide (PEO, Mw: 4 million), lithium bis(fluorosulfonyl)imide (LiFSI, 99%, PROVISCO, CS), and 1-butyl-1-methylpyrrolidinium bis(fluorosulfonyl)imide ($PYR_{14}FSI$, prepared following the procedure described in the literature [51]) were mixed in a ratio of 10:1:4. Benzophenone (BP, Acros Organics, 99+%) was added (5 wt% versus the amount of PEO) as photo-initiator for the cross-linking reaction. The obtained material was vacuum dried at 100 °C for 12 h. Finally, the soft and elastic electrolyte was hot-pressed at 100 °C – first at 10 t cm^{-2} for 3 min, then for 4 min each at 20, 30, and 50 tons cm^{-2} – to obtain very thin membranes with a thickness lower than 20 μm. These were cross-linked under UV light (Cube photo-irradiator, 350 W Hg lamp) for 6 min. The ionic liquid-based electrolyte (ILE) was prepared by dissolving lithium bis(trifluoromethanesulfonyl)imide (LiTFSI, battery grade, 99.5 wt%, 3 M) in $PYR_{14}FSI$ to achieve the $0.8PYR_{14}FSI$-0.2LiTFSI molar composition. The neat ionic liquid was pre-dried at 80 °C in a tubular vacuum oven and any remaining volatile compounds were removed at 80 °C using a turbomolecular pump ($p < 10^{-7}$ mbar).

Preparation of the NCM811-based electrodes: The NCM811-based electrodes were prepared by mixing the active material, the conductive carbon (Super C65, IMERYS), and polyvinylidene difluoride (PVdF, Solef 6020, Solvay) in a weight ratio of 92:4:4. The slurry with a solid content of ≥60% was prepared using *N*-methyl-2-pyrrolidone (NMP; anhydrous, >99.5%; Sigma-Aldrich) as dispersant/solvent, and cast onto aluminum foil (battery grade, thickness: 15 μm). After drying in the dry room (dew point of less than −60 °C) overnight, disk-shaped electrodes with a diameter of 12 mm were punched, vacuum-dried at 120 °C for 12 h, and finally pressed at 5 t cm^{-2}. The average active material mass loading was 2.7 ± 0.2 mg cm^{-2}, but preliminary tests on high areal loading (~12 mg cm^{-2}) were also performed.

Electrochemical measurements: All electrochemical measurements were performed in pouch cells, which were assembled in the dry room. One drop (≤5 μL cm^{-2}) of ILE was spread over both the cathode and the lithium metal. Galvanostatic cycling was performed by means of a Maccor battery tester 4300 in the voltage range from 3.0 to 4.3 V. The stripping/plating experiments, including the related electrochemical impedance spectroscopy (EIS) measurements, were performed using a VMP multichannel potentiostat (BioLogic) within the frequency range from 1 MHz to 10 mHz with a voltage amplitude of 5 mV. The conductivity of all electrolytes was evaluated from EIS measurements performed using Solartron 1260 within the frequency range from 1 MHz to 1 Hz with a voltage amplitude of 5 mV. For the Li//NCM811 cells dis-/charge rate of 1C corresponds to a specific current of 200 mA g^{-1} of NCM811. If not specified otherwise, all electrochemical measurements were performed in climatic chambers at 40 ± 2 °C. All voltage and potential values given herein refer to the lithium counter electrode as quasi-reference.

Materials characterization: The morphology of the different samples was investigated by scanning electron microscopy (SEM, ZEISS Crossbeam XB340 equipped with an energy dispersive X-ray (EDX) detector). All samples recovered from cycled cells were transferred to the microscope under argon atmosphere using an air-tight transfer box (Sample Transfer Shuttle, SEMILAB). X-ray photoelectron spectroscopy (XPS) measurements were performed on a Specs XPS system with a Phoibos 150 energy analyzer, using monochromatic Al K_α radiation (1486.6 eV), a take-off angle of 45°, and pass energies of 30 and 90 eV at the analyzer for the detail and survey spectra, respectively. For the sample preparation, the cycled electrodes were thoroughly washed with dimethyl carbonate (DMC), dried, and transferred under argon to the XPS system. The samples were either investigated directly or after Ar^+ ion sputtering for 30 min (~0.1 nm min^{-1} sputter rate, 0.03 μA, 5 kV). The software Casa XPS was utilized for the data analysis, using Shirley-type backgrounds and Gaussian-Lorentzian peak shapes. For the S2p peak, doublets with the expected intensity ratio (2:1) and spin-orbit splitting (1.2 eV) were used in the fit. All XPS spectra were calibrated to the C1s peak of the conductive carbon additive and/or adventitious carbon (C–C/C–H species) at 284.8 eV. X-ray diffraction (XRD) patterns were recorded on a Bruker D8 diffractometer equipped with a Cu Kα source ($\lambda = 0.15406$ nm) in the $10° < 2\theta < 90°$ range with a step size of 0.0205° and a 0.5s per point acquisition time. The thermo-gravimetric analyses (Discovery TGA, TA instruments) were carried out by sealing the investigated samples in aluminium pans (samples weight: ~12 mg for SE, ~1 mg for SPE), following an isothermal condition at 30 °C for 30 min, then heating up from 30 °C to 600 °C in artificial air atmosphere (heating ramp: 5 °C min^{-1}, the gas flow was containing N_2 and O_2 with the ratio of 4:1).

CRediT authorship contribution statement

Fanglin Wu: Data curation, Investigation, Writing – original draft. **Shan Fang:** Investigation. **Matthias Kuenzel:** Formal analysis, Writing – review & editing. **Thomas Diemant:** Formal analysis. **Jae-Kwang Kim:** Resources. **Dominic Bresser:** Funding acquisition, Writing – review & editing. **Guk-Tae Kim:** Conceptualization, Supervision. **Stefano Passerini:** Conceptualization, Funding acquisition, Writing – review & editing.

Declaration of competing interest

The authors declare that they have no known competing financial interests or personal relationships that could have appeared to influence the work reported in this paper.

Data availability

Data will be made available on request.

Acknowledgements

F.W. gratefully acknowledges the financial support from the Chinese Scholarship Council (CSC). The authors would like to acknowledge the financial support from the Helmholtz Association and the German Federal Ministry of Education and Research (BMBF) for funding within the LISI (03XP0224D) and the LILLINT (03XP0225D) project. Moreover, the authors would like to thank Dr. Xinpei Gao for preparing the ionic liquid, Xu Dong for her support with the TGA and DSC measurements, and Hyeongseon Choi for conducting the ICP measurements. J.-K.K. acknowledges the support from the National Research Foundation of Korea (NRF) grant funded by the Korean government (MSIT) (NRF-2020R1A2C2009057, NRF- 2021R1A4A200168711).

References

[1] S. Xia, X. Wu, Z. Zhang, Y. Cui, W. Liu, Chem 5 (2019) 753–785.
[2] B. Liu, J.-G. Zhang, W. Xu, Joule 2 (2018) 833–845.
[3] F. Wu, A.R. Schür, G.-T. Kim, X. Dong, M. Kuenzel, T. Diemant, G. D'Orsi, E. Simonetti, M. De Francesco, M. Bellusci, G.B. Appetecchi, S. Passerini, Energy Storage Mater. 42 (2021) 826–835.
[4] S. Jiao, X. Ren, R. Cao, M.H. Engelhard, Y. Liu, D. Hu, D. Mei, J. Zheng, W. Zhao, Q. Li, N. Liu, B.D. Adams, C. Ma, J. Liu, J.-G. Zhang, W. Xu, Nat. Energy 3 (2018) 739–746.
[5] X. He, D. Bresser, S. Passerini, F. Baakes, U. Krewer, J. Lopez, C.T. Mallia, Y. Shao-Horn, I. Cekic-Laskovic, S. Wiemers-Meyer, F.A. Soto, V. Ponce, J.M. Seminario, P. B. Balbuena, H. Jia, W. Xu, Y. Xu, C. Wang, B. Horstmann, R. Amine, C.-C. Su, J. Shi, K. Amine, M. Winter, A. Latz, R. Kostecki, Nat. Rev. Mater. 6 (2021) 1036–1052.
[6] L. He, C. Chen, M. Kotobuki, F. Zheng, H. Zhou, L. Lu, J. Mater. Chem. 7 (2019) 9748–9760.
[7] S. Yang, Z. Zhang, L. Shen, P. Chen, Z. Gu, M. Chang, Y. zhao, H. He, X. Yao, J. Power Sources 518 (2022).
[8] J. Yang, Z. Huang, P. Zhang, G. Liu, X. Xu, X. Yao, ACS Appl. Energy Mater. 2 (2019) 7299–7305.
[9] S. Duluard, A. Paillassa, L. Puech, P. Vinatier, V. Turq, P. Rozier, P. Lenormand, P.-L. Taberna, P. Simon, F. Ansart, J. Eur. Ceram. Soc. 33 (2013) 1145–1153.
[10] Q. Liu, Q. Yu, S. Li, S. Wang, L. Zhang, B. Cai, D. Zhou, B. Li, Energy Storage Mater. 25 (2020) 613–620.
[11] A. Paolella, W. Zhu, G.L. Xu, A. La Monaca, S. Savoie, G. Girard, A. Vijh, H. Demers, A. Perea, N. Delaporte, A. Guerfi, X. Liu, Y. Ren, C.J. Sun, J. Lu, K. Amine, K. Zaghib, Adv. Energy Mater. 10 (2020), 2001497.
[12] P. Hartmann, T. Leichtweiss, M.R. Busche, M. Schneider, M. Reich, J. Sann, P. Adelhelm, J. Janek, J. Phys. Chem. C 117 (2013) 21064–21074.
[13] H. Chung, B. Kang, Chem. Mater. 29 (2017) 8611–8619.
[14] J. Liu, H. Yuan, H. Liu, C.Z. Zhao, Y. Lu, X.B. Cheng, J.Q. Huang, Q. Zhang, Adv. Energy Mater. (2021), 2100748.
[15] Y. Liu, C. Li, B. Li, H. Song, Z. Cheng, M. Chen, P. He, H. Zhou, Adv. Energy Mater. 8 (2018).
[16] Y. Liu, Q. Sun, Y. Zhao, B. Wang, P. Kaghazchi, K.R. Adair, R. Li, C. Zhang, J. Liu, L. Y. Kuo, Y. Hu, T.K. Sham, L. Zhang, R. Yang, S. Lu, X. Song, X. Sun, ACS Appl. Mater. Interfaces 10 (2018) 31240–31248.
[17] Q. Yu, D. Han, Q. Lu, Y.B. He, S. Li, Q. Liu, C. Han, F. Kang, B. Li, ACS Appl. Mater. Interfaces 11 (2019) 9911–9918.
[18] Z. Zhang, S. Chen, X. Yao, P. Cui, J. Duan, W. Luo, Y. Huang, X. Xu, Energy Storage Mater. 24 (2020) 714–718.
[19] C.-Z. Zhao, B.-C. Zhao, C. Yan, X.-Q. Zhang, J.-Q. Huang, Y. Mo, X. Xu, H. Li, Q. Zhang, Energy Storage Mater. 24 (2020) 75–84.
[20] P. Oh, H. Lee, S. Park, H. Cha, J. Kim, J. Cho, Adv. Energy Mater. 10 (2020).
[21] Q. Zhou, J. Ma, S. Dong, X. Li, G. Cui, Adv. Mater. 31 (2019), e1902029.
[22] I. Osada, H. de Vries, B. Scrosati, S. Passerini, Angew. Chem. Int. Ed. 55 (2016) 500–513.
[23] L. Xu, J. Li, H. Shuai, Z. Luo, B. Wang, S. Fang, G. Zou, H. Hou, H. Peng, X. Ji, J. Energy Chem. 67 (2022) 524–548.
[24] S.A. Pervez, G. Kim, B.P. Vinayan, M.A. Cambaz, M. Kuenzel, M. Hekmatfar, M. Fichtner, S. Passerini, Small 16 (2020), e2000279.
[25] J.S. Thokchom, B. Kumar, J. Power Sources 195 (2010) 2870–2876.
[26] B. Kumar, D. Thomas, J. Kumar, J. Electrochem. Soc. 156 (2009).
[27] J.S. Thokchom, B. Kumar, J. Power Sources 185 (2008) 480–485.
[28] B. Kumar, J.S. Thokchom, J. Am. Ceram. Soc. 90 (2007) 3323–3325.
[29] S. Brutti, E. Simonetti, M. De Francesco, A. Sarra, A. Paolone, O. Palumbo, S. Fantini, R. Lin, A. Falgayrat, H. Choi, M. Kuenzel, S. Passerini, G.B. Appetecchi, J. Power Sources 479 (2020), 228791.
[30] Z. Sun, L. Liu, B. Yang, Q. Li, B. Wu, J. Zhao, L. Ma, Y. Liu, H. An, Solid State Ionics 346 (2020), 115224.
[31] L. Xu, S. Tang, Y. Cheng, K. Wang, J. Liang, C. Liu, Y.-C. Cao, F. Wei, L. Mai, Joule 2 (2018) 1991–2015.
[32] J. Kalhoff, G.G. Eshetu, D. Bresser, S. Passerini, ChemSusChem 8 (2015) 2154–2175.
[33] Z. Chen, G.T. Kim, J.K. Kim, M. Zarrabeitia, M. Kuenzel, H.P. Liang, D. Geiger, U. Kaiser, S. Passerini, Adv. Energy Mater. 11 (2021), 2101339.
[34] F. Wu, G.T. Kim, T. Diemant, M. Kuenzel, A.R. Schür, X. Gao, B. Qin, D. Alwast, Z. Jusys, R.J. Behm, D. Geiger, U. Kaiser, S. Passerini, Adv. Energy Mater. 10 (2020), 2001830.
[35] F. Wu, S. Fang, M. Kuenzel, A. Mullaliu, J.-K. Kim, X. Gao, T. Diemant, G.-T. Kim, S. Passerini, Joule 5 (2021) 2177–2194.
[36] G. Hou, X. Ma, Q. Sun, Q. Ai, X. Xu, L. Chen, D. Li, J. Chen, H. Zhong, Y. Li, Z. Xu, P. Si, J. Feng, L. Zhang, F. Ding, L. Ci, ACS Appl. Mater. Interfaces 10 (2018) 18610–18618.
[37] Z. Zhang, L. Zhang, Y. Liu, H. Wang, C. Yu, H. Zeng, L.M. Wang, B. Xu, ChemSusChem 11 (2018) 3774–3782.
[38] S. Xiong, Y. Liu, P. Jankowski, Q. Liu, F. Nitze, K. Xie, J. Song, A. Matic, Adv. Funct. Mater. 30 (2020), 2001444.
[39] J. Tan, X. Ao, A. Dai, Y. Yuan, H. Zhuo, H. Lu, L. Zhuang, Y. Ke, C. Su, X. Peng, B. Tian, J. Lu, Energy Storage Mater. 33 (2020) 173–180.
[40] T.C. Mendes, N. Goujon, N. Malic, A. Postma, J. Chiefari, H. Zhu, P.C. Howlett, M. Forsyth, J. Electrochem. Soc. 167 (2020), 070525.
[41] J. Tang, L. Wang, C. Tian, C. Chen, T. Huang, L. Zeng, A. Yu, ACS Appl. Mater. Interfaces 14 (2022) 4170–4178.
[42] J. Wan, J. Xie, X. Kong, Z. Liu, K. Liu, F. Shi, A. Pei, H. Chen, W. Chen, J. Chen, X. Zhang, L. Zong, J. Wang, L.Q. Chen, J. Qin, Y. Cui, Nat. Nanotechnol. 14 (2019) 705–711.
[43] B. Yuan, B. Zhao, Q. Wang, Y. Bai, Z. Cheng, Z. Cong, Y. Lu, F. Ji, F. Shen, P.-F. Wang, X. Han, Energy Storage Mater. 47 (2022) 288–296.
[44] H. Huo, Y. Chen, R. Li, N. Zhao, J. Luo, J.G. Pereira da Silva, R. Mücke, P. Kaghazchi, X. Guo, X. Sun, Energy Environ. Sci. 13 (2020) 127–134.
[45] T. Jiang, P. He, G. Wang, Y. Shen, C.W. Nan, L.Z. Fan, Adv. Energy Mater. 10 (2020), 1903376.
[46] J. Hu, P. He, B. Zhang, B. Wang, L.-Z. Fan, Energy Storage Mater. 26 (2020) 283–289.
[47] F. He, W. Tang, X. Zhang, L. Deng, J. Luo, Adv. Mater. 33 (2021), e2105329.
[48] M.J. Lee, J. Han, K. Lee, Y.J. Lee, B.G. Kim, K.N. Jung, B.J. Kim, S.W. Lee, Nature 601 (2022) 217–222.
[49] H. Wan, S. Liu, T. Deng, J. Xu, J. Zhang, X. He, X. Ji, X. Yao, C. Wang, ACS Energy Lett. 6 (2021) 862–868.
[50] C. Xu, B. Sun, T. Gustafsson, K. Edström, D. Brandell, M. Hahlin, J. Mater. Chem. 2 (2014) 7256–7264.
[51] M. Montanino, F. Alessandrini, S. Passerini, G.B. Appetecchi, Electrochim. Acta 96 (2013) 124–133.